ADVANCED MATERIALS INTERFACES
Open Access
www.advmatinterfaces.de

Local Manipulation of the Energy Levels of 2D TMDCs on the Microscale Level via Microprinted Self-Assembled Monolayers

Sarah Grützmacher, Max Heyl, Marco Vittorio Nardi, Norbert Koch, Emil J. W. List-Kratochvil, and Giovanni Ligorio**

2D transition metal dichalcogenides (TMDCs) are atomically-thick semiconductors with great potential for next-generation optoelectronic applications, such as transistors and sensors. Their large surface-to-volume ratio makes them energy-efficient but also extremely sensitive to the physical-chemical surroundings. The latter must be carefully considered when predicting the electronic behavior, such as their energy level alignment, which ultimately affects the charge carrier injection and transport in devices. Here, local doping is demonstrated and thus adjusting the opto-electronic properties of monolayer TMDCs (WSe_2 and MoS_2) by chemically engineering the surface of the supporting substrate. This is achieved by decorating the substrate by microcontact printing with patterns of two different self-assembled monolayers (SAMs). The SAMs posses distinct molecular dipoles and dielectric constants, significantly influencing the TMDCs electronic and optical properties. By analyzing (on various substrtates), it is confirmed that these effects arise solely from the interaction between SAMs and TMDCs. Understanding the diverse dielectric environments experienced by TMDCs allows for a correlation between electronic and optical behaviours. The changes primarily involve alteration in the electronic band gap width, which can be calculated using the Schottky-Mott rule, incorporating the dielectric screening of the TMDCs surroundings. This knowledge enables accurate prediction of the (opto-)electronic behavior of monolayer TMDCs for advanced device design.

1. Introduction

Due to unique optical and electronic properties, 2D transition metal dichalcogenides (TMDCs) are emerging as a potential alternative to silicon technology for next generation opto- and nano-electronic applications.[1–3] When going from the 3D bulk to the 2D monolayer (ML), TMDCs transition from indirect to direct band gap semiconductors, enabling (semi-)transparent and mechanically flexible architectures.[4,5] This renders them promising materials for device applications spanning all realms of electronics and optoelectronics. It is the atomic-scale thickness of the TMDCs that allows for ultra-short channels and hence energy-efficient field-effect transistors for integrated circuits.[6] Their ability to transport both electrons and holes opens the door to new design opportunities for ambipolar logic electronics.[7–9] Furthermore, TMDCs exhibit exotic physics such as unconventional quantum Hall effect and quantum transport phenomena,[10] valley degrees of freedom,[11,12] and complex exciton physics[3,12–16]

S. Grützmacher, M. Heyl, N. Koch, E. J. W. List-Kratochvil, G. Ligorio
Humboldt-Universität zu Berlin
Institut für Physik
Institut für Chemie
IRIS Adlershof
Zum Großen Windkanal 2, 12489 Berlin, Germany
E-mail: emil.list-kratochvil@hu-berlin.de; giovanni.ligorio@hu-berlin.de

The ORCID identification number(s) for the author(s) of this article can be found under https://doi.org/10.1002/admi.202300276

DOI: 10.1002/admi.202300276

M. V. Nardi
IMEM-CNR Institute of Materials for Electronics and Magnetism
Via Alla Cascata 56/C, Povo, Trento 38123, Italy

N. Koch, E. J. W. List-Kratochvil
Helmholtz-Zentrum Berlin für Materialien und Energie GmbH
Hahn-Meitner-Platz 1, 14109 Berlin, Germany

The doping techniques for the 3D bulk silicon, established over the past seven decades,[17] allows for the transition from intrinsic-to-extrinsic semiconductor nature, which is necessary for modern day technologies. Before TMDCs are ready to substitute silicon in electronic applications, suitable doping techniques for 2D materials must be found. Due to the large surface-to-volume ratio of 2D TMDCs "the interface is the device." Changing the interface between the TMDC and its environment has a drastic effect on the TMDC's electric and optical behavior, such as their work function(Φ),[18–26] their electronic band gap (E_g),[15,16,27–30] and their photoluminescence (PL).[31–35]

The tuning of the physico-chemical interactions that occur between the TMDC and substrate is a practical approach to design high-performance TMDC-based devices.[21,22,24,32,36] An interface-mediated doping can be achieved via chemical modification of the substrate supporting the TMDC. For this, self-assembled monolayers (SAMs), that is, densely packed organic surfactants with a thickness of a single molecular layer, prove to be a promising candidate. This simple and low-cost approach lies in the wide spectrum of commercially available SAMs, where the anchoring group can be chosen to match the substrate and the molecular structure determines the interaction with the TMDC. Shown when the chemical structure of the SAM-molecule can carry a permanent electric dipole, whose average orientation determines the electrostatic potential landscape of the substrate surface.[23,25,37,38] Depending on the dipole orientation, the Fermi Level (E_F) of the TMDC transferred on the modified substrate is shifted within the E_g.[18] In case of an upward dipole orientation, the E_F is shifted toward the conduction band, thereby increasing the electron concentration in the TMDC. A downward dipole orientation shifts the E_F toward the valence band, increasing the hole concentration. However, the surface dipole of the SAMs does not only shift E_F of the TMDC but also has a profound effect on the TMDC carrier mobility, the Coulomb interaction potential between electrons and holes, varying the exciton binding energies, and the electronical band gap; This is due to dielectric mismatch between the 2D semiconductor and its environment.[39,40] Therefore, to predict the substrate dependent electronic and optical behavior of the TMDC the influence of the dielectric environment must be carefully considered.

In this work, we demonstrate that the electronic and optical behavior of the TMDCs results from the combined effects of electrostatic surface potentials and dielectric screening. We demonstrate the importance of understanding the interaction at the TMDC/substrate interface to correctly predict this behavior. For this purpose, we investigated WSe_2 and MoS_2 on two different substrates modified with two different SAMs. We show that both electrical and optical behaviors are modified by the SAMs and that the modulation of the dielectric environment must be taken into consideration for a comprehensive understanding of the observed phenomena.

2. Results and Discussion

2.1. Lateral Functionalization of Substrates with SAMs

Microcontact printing (μCP) was employed as tool for the surface modification of the substrates (Si/SiO_2 wafers, 300 nm oxide layer) to achieve microscale lateral features of two different SAMs. The reader is referred to the Experimental Section for details regarding the sample preparation and measurement procedures.

Figure 1a shows a schematic representation of the μCP process of octodecytrichlor-silane (OTS) and the chemical structure of the SAM-molecule. OTS ($CH_3(CH_2)_{17}SiCl_3$) consists of a C_{18} carbohydrate chain with an anchoring silane group, which is ideal to bind to the Si/SiO_2 substrate. The molecule exhibits a length of 2.4 nm.[38] The chemical modification of the substrate was investigated using scanning force microscopy (SFM). Figure 1b displays the SFM image of the modified substrate, where the printed features of the OTS-SAM have a 10 μm line width, corresponding to the topography of the PDMS stamp. The SAM lines are elevated with respect to the surface of the substrate by 1.1 nm. The inset line in the image reports the height that was measured locally. The thickness of the ML was reproducible both from batch to batch as well as within each batch, with a variance of ±0.1 nm. The discrepancy between the theoretical length of the molecule (2.4 nm) and the SAM-height, which has been experimentally measured (in our case 1.1 nm) has often been reported in literature.[38,41,42] This is usually attributed to two main causes. The first is the tilt angle of the molecules with respect to the surface, which depends on the density of the SAM. The second results from measurement underestimation of the thickness. For this task SFM is a common experimental method employed but seems to systematically display lower values for the SAM-height. This has been attributed to measurement artifacts arising from the different adhesion forces experienced by the SFM cantilever on OTS with respect to SiO_2, the former being hydrophobic and the latter hydrophilic.[38] To be certain that the SAM fabricated via μCP has the same effect on the substrate surface, specifically the surface energy, as high-density SAMs produced via chemical bath deposition, we experimentally compared samples fabricated with the two different methods via contact angle measurements (CA). For the sample fabricated via chemical bath deposition, a Si/SiO_2 substrate (cleaned via sonication and treated via oxygen plasma to activate the surface) was immersed overnight into an OTS solution. The sample produced via μCP was prepared with a stamp with no features to achieve full coverage of the sample. The CA measured for the two samples is 111.7° ± 0.2° and 109.5° ± 0.4°, respectively (see Figure S1, Supporting Information). Although the μCP sample displays a slightly smaller CA with respect to the CBD sample, both values are in good agreement with literature values for OTS deposited via CBD, which have been measured around 110°.[43–46] Values for vapor-deposited OTS are typically lower, due to less compactness of the SAM, and are measured around 100°.[47,48] Therefore, despite the small difference in the CA between the two samples, we consider the change in surface energy of the substrate (and hence the achieved coverage) to be very similar for both μCP and CBD samples.

The presence of the OTS-SAM was additionally confirmed via X-ray photoemission spectroscopy (XPS), performed on substrates printed in an analogous way. To meet the lateral detection limitation of XPS, stamps without features were employed for full coverage of the substrate. To avoid substrate charging during the measurements, highly doped Si substrates with a native oxide layer (≈ 3 nm) were chosen.

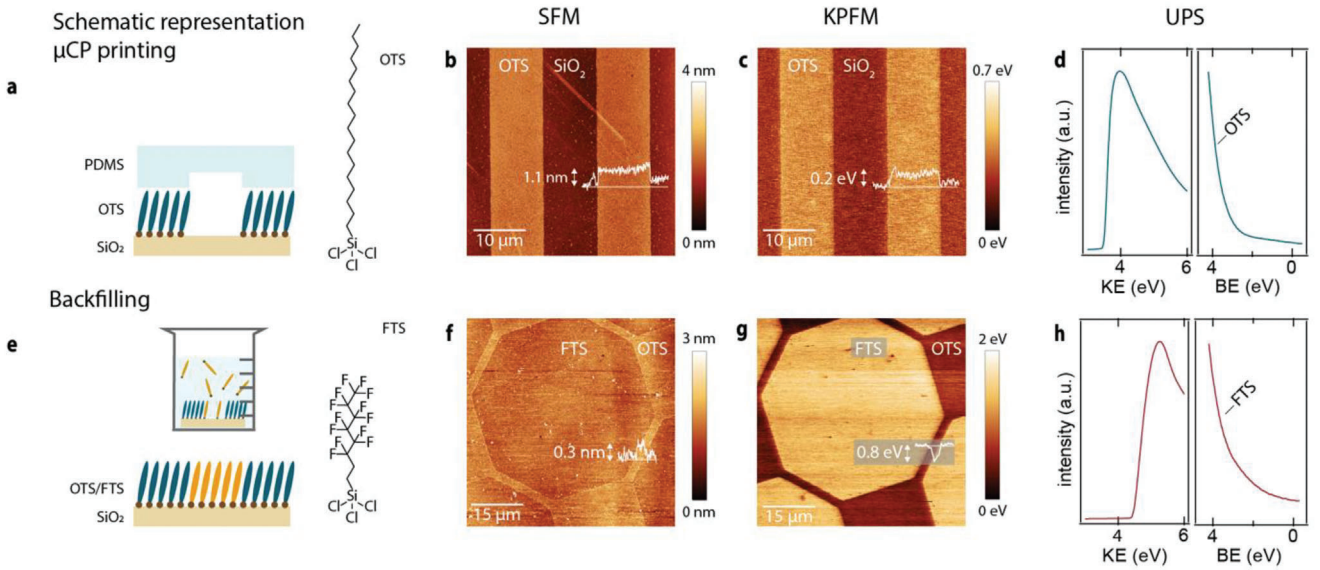

Figure 1. a,e) Schematic of microcontact printing of OTS and its chemical structure; backfilling via chemical bath deposition of FTS. b,f) SFM image of OTS-SAM and OTS/FTS-SAM pattern, respectively. The inset lines represent the height measured locally. c,g) KPFM images of OTS-SAM and OTS/FTS-SAM pattern, displaying a difference in CPD of $\Delta^{KPFM}_{SiO2-OTS} = -0.2$ eV and $\Delta^{KPFM}_{FTS-OTS} = 0.8$ eV, respectively. The inset lines represent the CPD measured locally. d,h) Secondary electron cutoff (SECO) and valence band spectra of OTS and FTS on native SiO_2 oxide, respectively. The difference in work function for the two SAMs on SiO_2 is $\Delta^{SECO}_{FTS-OTS} = 1$ eV.

To investigate the electrical modification of the substrate by the SAM, Kelvin probe force microscopy (KPFM) was performed. Figure 1c shows the KPFM image acquired simultaneously during the SFM image, reported in Figure 1b. The SAM pattern is confirmed in contrast to the contact potential difference (CPD). OTS exhibits a larger CPD compared to SiO_2 with $\Delta^{KPFM}_{SiO_2-OTS} = -0.2$ eV, which is in good agreement with literature values[38] The inset line in the image displays the CPD measured locally. To gain further information about the electronic properties of the SAM-modified surface, the secondary electron cutoff (SECO) and valence band (VB) were investigated via ultraviolet photoemission spectroscopy (UPS). These measurements were performed on the same substrates investigated via XPS (see above). Figure 1d displays the SECO and VB spectra of OTS, from which the work function (Φ_{OTS} = 3.5 eV) and the hole injection barrier (HIB = 2.4 eV) were extrapolated.

After the successful patterning of OTS, the second SAM was deposited into the gaps via backfilling. This was achieved by immersing OTS-patterned substrates into a trichloro(1,1,2,2-perfluorooctyl)silane (FTS) solution. Figure 1e shows the backfilling procedure and the chemical structure of the molecule. FTS ($CF_3(CF_2)_5(CH_2)_2SiCl_3$) consists of a perflourated C_6 carbon chain, a $(-CH_2)_2$ spacer group and an anchoring silane group. The molecule exhibits a length of 1.4 nm[49–51] In order to clearly differentiate the two SAMs, the following results report samples fabricated employing a stamp with an asymmetric pattern. The OTS-SAM is printed in squares (20 × 20 μm^2), connected diagonally by lines (2 μm width). The FTS-SAM fills the octagonal gaps. Figure 1f shows the SFM image, where the OTS-SAM is visible in the elevated brighter areas, as expected by the larger length of the OTS (C_{18}) with respect to the FTS (C_8) molecule. The inset line in the image displays the height measured locally and shows a difference of 0.3 nm between the two SAMs. Given the height of 1.1 nm measured for OTS, the height of FTS can be calculated to be 0.8 nm. This is in good agreement with literature values, where FTS is reported to form an ML of 0.9–1 nm.[49–51] Additionally, the result was reproducible with a variance of ±0.1 nm from batch to batch. To prove that the pattern has high quality over a large area, images were taken with scanning electron microscopy at a larger scale at random positions on the substrate. Typical images can be found in Figure S2, Supporting Information.

XPS was performed on FTS-treated, highly doped Si substrates with a native oxide layer. The results (for both OTS and FTS) can be found in the supplementary information (Figure S3, Supporting Information) and report the spectra for carbon [C(1s)] and fluorine [F(1s)]. For OTS the C(1s) core level consists of one peak centered at 287 eV, attributed to the $-CH_2$ and $-CH_3$ carbons. For FTS the C(1s) core level consists of two main components with binding energies at 287 eV and 293 eV, which are assigned to the $-CH_2$ and $-CF_2/-CF_3$ groups, respectively.

Figure 1g displays the KPFM image acquired simultaneously during the SFM image reported in Figure 1f. The two SAM regions are clearly discernible, as the FTS-SAM exhibits a larger CPD compared to the OTS-SAM ($\Delta^{KPFM}_{FTS-OTS} = 0.8$ eV). The inset line in the image displays the CPD measured locally. To confirm these results, UPS was performed on FTS on Si/SiO_2 (native oxide) substrates, analogously prepared to those of OTS. The SECO and VB spectra can be seen in Figure 1h. The obtained values (Φ_{FTS} = 4.5 eV, HIB = 1.3 eV) are in good agreement with the KPFM measurements ($\Delta^{SECO}_{FTS-OTS} = 1$ eV).

The ability of SAMs to change the work function (Φ) of a substrate is due to the change of the surface dipole induced by their electrostatic potential. Every adsorbed species with a permanent

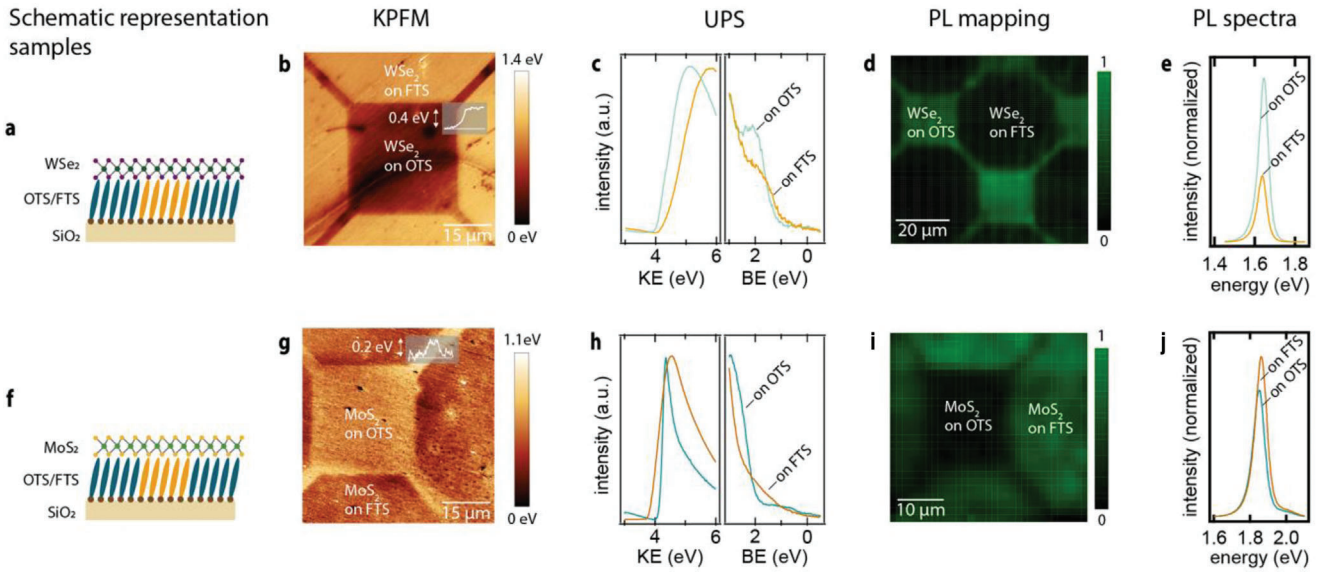

Figure 2. a,f) Schematic of the cross section of the prepared samples. SiO_2 substrates with OTS- and FTS-SAM pattern with TMDCs transferred on top. The topmost part of the figure refers to WSe_2, while the bottommost to MoS_2. b,g) KPFM images of the samples showing the SAM pattern, displaying a difference in CPD of $\Delta^{WSe_2}_{FTS-OTS} = 0.4$ eV and $\Delta^{MoS_2}_{FTS-OTS} = -0.2$ eV. The inset lines represent the CPD measured locally. c,h) UPS (secondary electron cutoff and valence band spectra) of WSe_2 and MoS_2 transferred on OTS and FTS. d,i) PL map of WSe_2 and MoS_2 transferred on OTS/FTS pattern. The brightness of every pixel represents the local PL intensity integrated between 1.4–1.9 eV and 1.6–2.1 eV, respectively. e,j) Averaged PL spectra of WSe_2 and MoS_2 on OTS and FTS.

dipole causes a change in the work function, according to the Helmholtz equation:

$$\Delta\Phi_{sub} = \frac{qN\mu_z}{\epsilon_0\epsilon_{SAM}} \quad (1)$$

where $\Delta\Phi_{sub}$ represents the change in ϕ of the substrate induced by the SAM, q the elementary charge, N the packing density, μ_z the permanent dipole moment of the SAM perpendicular to the surface, ϵ_0 the permittivity of free space and ϵ_{SAM} the relative permittivity.[22,38] Due to the strongly polar C–F bond compared to the lightly polar C–H bond, perflourated molecules, such as FTS, display a larger, downward orientated molecular dipole moment. The value of a comparable molecule $(CF_3(CF_2)_7(CH_2)_2Si(OCH_3)_3)$, which is longer by only two $-CF_2$ groups than our FTS molecule, is $\mu_{FSAM} = 3.41$ D. OTS, on the other hand, displays an upward orientated molecular dipole moment with a value of $\mu_{OTS} = 0.94$ D.[38] The difference in direction and magnitude of the dipole moments of the two molecules explains the larger shift in Φ_{sub} induced by FTS compared to OTS. The experimental results are in good agreement with calculated values for Equation (1), considering values from literature for N, μ_{SAM} and ϵ_{SAM} (for OTS and FTS, see also below for further detail on ϵ). A schematic of the effect of the direction and magnitude of the dipole orientation of the SAMs to the Φ_{sub} is shown in Figure S4, Supporting Information.

It can be concluded that the work function of the substrate was successfully modified by the deposition of two different SAMs with different dipole moments. The influence of the surface modification on transferred TMDCs was investigated next.

2.2. Work Function and Photoluminescence Modulation of TMDCs by SAMs

ML WSe_2 was transferred onto the SAM-patterned substrates to investigate the effect of the SAMs on their electronic and optical properties. ML-WSe_2 were obtained following the previously reported thermally activated metal-mediated exfoliation process.[52,53] The presence and quality of the WSe_2 MLs were confirmed via Raman spectroscopy and optical microscopy (Figures S5 and S6, Supporting Information). The Raman spectra displays the in-plane vibration E^1_{2g} and the out-of-plane vibration A_{1g} frequency, which is typical for ML WSe_2, centered at 248.5 and 260.7 cm^{-1}, respectively. **Figure 2**a displays a schematic representation of the side view of the sample consisting of the Si/SiO_2 substrate, patterned with OTS/FTS-SAMs and ML-WSe_2.

KPFM measurements were performed to gain information about SAM-induced changes in the work function of WSe_2. Figure 2b shows the KPFM image of WSe_2 deposited on the OTS/FTS square pattern (shown in Figure 1f,g). The presence of the SAM pattern underneath the ML-WSe_2 is clearly visible in the contrast in the color-mapped CPD. The darker squared area corresponds to WSe_2 on OTS and the brighter area to WSe_2 on FTS. The inset line in the image is the CPD measured locally. The difference between the two areas is $\Delta\Phi^{WSe_2}_{FTS-OTS} = 0.4$ eV. To ensure that the measured CPD originates solely from the interaction between WSe_2 and the SAMs, and is independent from the substrate, the measurements were repeated on a different insulating substrate, Al_2O_3. The results on Al_2O_3 are in perfect agreement with those on Si/SiO_2 and are reported in the SI (Figure S7, Supporting Information). Hence, it is demonstrated that the change in the work function of WSe_2 (Φ^{WSe_2}) originates

from the ML/SAM interaction, as it has previously been reported by others.[22,25,26,36,39,54–57]

Quantitative information about the change of Φ^{WSe_2} on OTS and FTS was gained via UPS measurements. For this, OTS and FTS were deposited on highly doped Si substrates with a native oxide layer before ML-WSe_2 was transferred on top. From the SECO measurements, which are displayed on the left side of Figure 2c, the work function $\Phi_{FTS}^{WSe_2} = 4.3$ eV and $\Phi_{OTS}^{WSe_2} = 4.0$ eV are obtained. The difference in $\Phi_{FTS}^{WSe_2}$ compared to $\Phi_{OTS}^{WSe_2}$ of 0.3 eV is in excellent agreement with the KPFM measurements. From the VB measurements (right side of Figure 2c) the hole injection barrier $HIB_{FTS}^{WSe_2} = 0.9$ eV and $HIB_{OTS}^{WSe_2} = 1.1$ eV are extrapolated.

The values of HIB, which correspond to the difference between the VB onset and E_F, can be used to predict the n-/p-nature of a semiconductor if the value of E_g is known. For bulk semiconductors, such as silicon or organic thin film interface phenomena do not affect the n-/p-nature of the material. Therefore, E_g can be assumed constant and independent from the environment. In contrast, for 2D-semiconductors the chemical environment has a profound effect on the electronic structure such that E_g is strongly affected by interface phenomena of the substrate. It has been demonstrated that the dielectric properties of the substrate strongly influence the electronic energy levels of TMDCs, such as Φ, HIB and E_g.[16,21,27,31,34,40,58] For this reason, a large range of values for E_g of 2D-TMDCs can be found in literature, and in the case of WSe_2, it ranges from 1.60–1.95 eV. Consequently, choosing only one value for E_g to estimate the n-/p-nature of WSe_2 on both OTS and FTS would lead to a wrong prediction, as the specific environment must be regarded.

In a previous report,[30] we were able to accurately predict changes in E_g of MoS_2 due to substrate-induced dielectric screening by extending the Schottky–Mott rule. The Schottky–Mott rule in its simplest form approximates the Schottky barrier heights (Φ_B), which are the potential energy barriers formed at a metal-semiconductor interface between the metal work function and the edges of the valence and conductions bands of the semiconductor.[59] The sum of the two potential barriers corresponds to E_g. Despite the correct prediction of the band bending at the metal-semiconductor interface, the Schottky–Mott model has experimentally been shown to give false predictions, when used for TMDCs. This is due to fact that the model does not take physiochemical interactions between the metal and the semiconductor into consideration. These are largely enhanced in TMDCs in the ML limit, due to the largest surface-to-volume ratio.[15,16,28,29] The prediction of the E_g based on the Schottky–Mott rule must therefore be corrected with a term that considers these interactions and is expressed by:

$$E_g(\epsilon_r) = E_g(\epsilon_r = \infty) + \alpha/\epsilon_r \quad (2)$$

where $E_g(\epsilon_r)$ is the band gap of TMDC material on a substrate with the dielectric constant ϵ_r, $E_g(\epsilon_r = \infty)$ is the single-particle band gap of the TMDC on a substrate with infinite dielectric constant ($\epsilon_r = \infty$) and α is an empirical constant. Employing the extended Schottky–Mott rule we were able to predict with an excellent accuracy the E_g of MoS_2 on both metallic and insulating substrates.[30] Based on these findings, we cannot simply take values for the E_g of WSe_2 from literature, nor can we assume E_g to be constant on the two, chemically extremely different SAMs.

Table 1. Calculation of the energy level of WSe_2 and MoS_2 on OTS and FTS considering the expanded Schottky–Mott rule. Values for E_g ($\epsilon_r = \infty$) are taken from literature.[60] $E_g(\epsilon_r)$ was calculated according to Formula 2. All values are given in eV.

	Φ	HIB	$E_g(\epsilon_r = \infty)$	$E_g(\epsilon_r)$	EIB	½ $E_g(\epsilon_r)$	Δ
WSe_2 OTS	4.0	1.1	1.75	2.10	1.00	1.05	−0.05
WSe_2 FTS	4.3	0.9	1.75	2.25	1.35	1.13	0.23
MoS_2 OTS	4.0	2.0	1.90	2.24	0.25	1.12	−0.88
MoS_2 FTS	3.8	2.0	1.90	2.40	0.40	1.20	−0.80

Table 1 reports the energy level values for WSe_2 (and MoS_2, see below) on the two different SAMs. The work function Φ of the TMDCs on the two different SAMs is obtained via UPS (SECO onset). The HIB is also obtained via UPS. The electron injection barrier (EIB) is calculated as the difference between the calculated value of $E_g(\epsilon_r)$ and the measured HIB. The calculation of $E_g(\epsilon_r)$ is based on the extended Schottky–Mott rule. The values for $E_g(\epsilon_r = \infty)$ are taken from literature considering TMDCs on metal (1.75 eV for WSe_2 and 1.90 eV for MoS_2).[60] The empirical value α is 0.9 eV for MoS_2.[30] Due to similar polarizabilities of We and Mo and Se and S, we use the same value for WSe_2. Literature values for ϵ_r for OTS range from 2.3–3.0, and those for FTS from 1.7–1.9.[61–64] Calculating $E_g(\epsilon_r)$ for WSe_2 with the extended Schottky–Mott rule we obtain values of 2.10 ± 0.05 eV for OTS and 2.25 ± 0.03 eV for FTS. See below for the calculations for MoS_2.

In an intrinsic semiconductor the E_F lies in the middle of the band gap (we indicate this value with the symbol ½ E_g). Hence, to obtain quantitative information about the different doping levels of the TMDC on the SAMs we calculated the difference between ½ E_g and the HIB, which we call Δ. The closer the absolute value is to zero, the more intrinsic the TMDC is. A positive value corresponds to a p-doped TMDC, while a negative value to that of an n-doped TMDC.

With the calculated values for $E_g(\epsilon_r)$, we obtain Δ = −0.04 eV for WSe_2 on OTS Δ = 0.23 eV for WSe_2 on FTS. Thus, WSe_2 is p-doped on FTS and intrinsic on OTS. **Figure 3**a schematically summarizes the energy level discussed above.

To confirm these results, PL measurements were performed. The PL originates from the radiative relaxation of photogenerated electron-hole pairs (excitons). If the TMDC is p- or n-doped, an additional hole or electron can bind to the exciton, generating a trion, which decreases the PL intensity.[32,33,35,65,66] Thus, there is a direct correlation between the doping level of a TMDC and its PL intensity. The intensity has its maximum for an intrinsic TMDC and decreases with increasing p/n-doping.

Figure 2d shows the PL map of WSe_2 deposited on the SAMs. Each pixel of the image represents the local PL intensity integrated between 1.4 and 1.9 eV. The SAM pattern is visible in an enhanced PL intensity of WSe_2 on the OTS-SAM. Figure 2e shows the averaged PL spectra (over a region of 20 × 20 μm²) for WSe_2 on FTS and OTS. The PL intensity for WSe_2 on OTS is approximately twofold larger than that of WSe_2 on FTS, indicating that WSe_2 on FTS has a higher trion to exciton ratio.

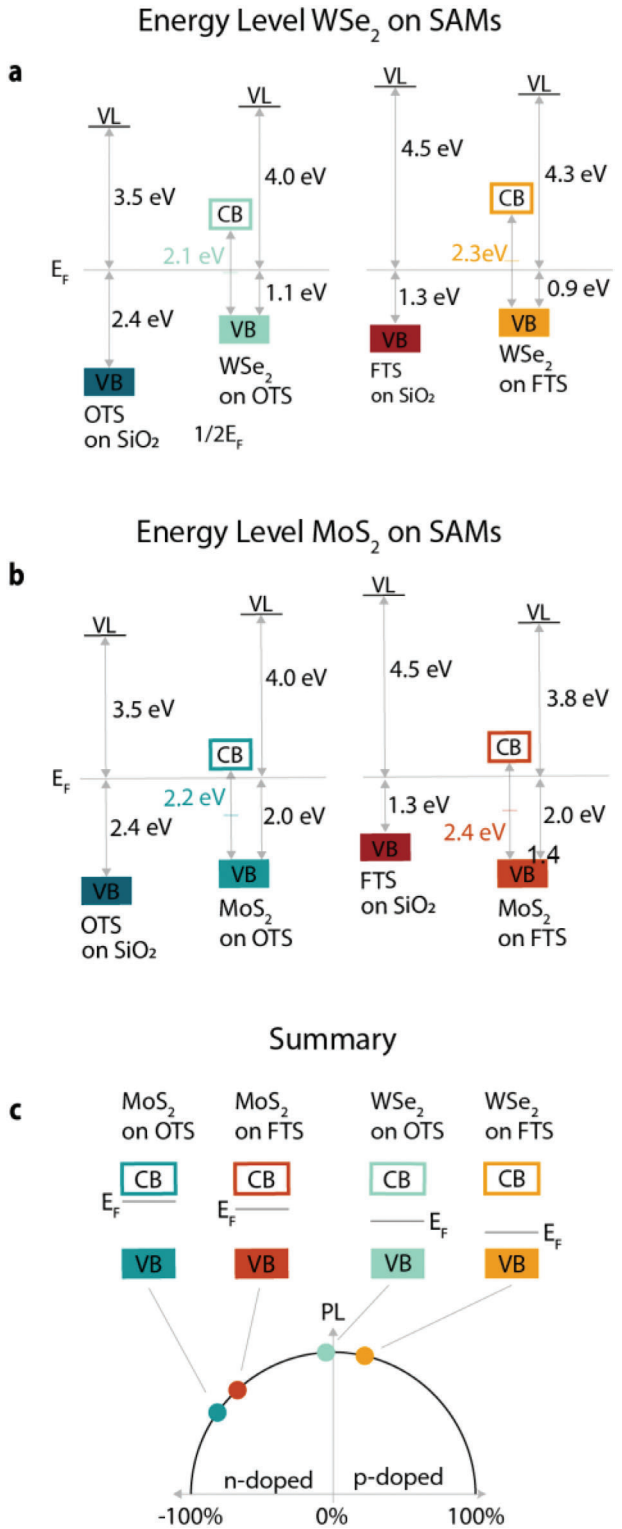

Figure 3. a,b) Schematic of the energy level of WSe_2 and MoS_2, respectively, on OTS- and FTS-SAM. c) Schematic of the correlation between the PL intensity and the doping level of WSe_2 MoS_2. The PL intensity decreases with increased doping level for both TMDCs.

This suggests a more intrinsic nature for WSe_2 on OTS with respect to WSe_2 on FTS. This is confirmed by the peak deconvolution displayed in Figure S8, Supporting Information and summarized in Table S1, Supporting Information. The PL signal was deconvoluted into two peaks. The main peak is attributed to the neutral exciton peak denoted as X^0 and the smaller peak is attributed to the either negatively or positively charged trion peak, denoted as X^- and X^+. UPS measurements indicate on OTS a close to intrinsic, yet slightly n-doped character for WSe_2. Hence, the PL deconvolves in a X^0 peak and a small X^- peak. The X^- peak is redshifted with respect to the X^0 peak by 45 meV. UPS measurements indicate on FTS a p-doped character for WSe_2. We therefore deconvolve the PL in a X^0 peak and a positively charged trion peak X^+. The X^+ peak is redshifted with respect to the X^0 peak by 30 meV. It can be noted that although the main peak stays almost in the same position, the peak attributed in the trions changes in position by 15 meV, which we associate with the different (negatively/positively charged) trion nature. As Δ for OTS is almost zero, indicating that the E_F lies at $\frac{1}{2}E_g$, while Δ for FTS is 0.23, indicating that the E_F lies above $\frac{1}{2}E_g$, predicting a p-doped character. Figure 3c schematically summarizes the correlation between the PL intensity and the n-/p-nature.

To confirm our results all experiments were repeated with MoS_2. Figure 2f displays a schematic of the side view of the sample. Analogous to the WSe_2, MoS_2 was transferred onto OTS/FTS patterned Si/SiO_2 substrates. The quality of the MoS_2 MLs was ensured via Raman spectroscopy and optical microscopy (Figures S5 and S6, Supporting Information). The Raman spectra show the in-plane vibration E^1_{2g} and the out-of plane vibration A_{1g} frequency, which is typical for ML MoS_2, centered at 390.2 and 408.5 cm^{-1}, respectively. Figure 2g displays the KPFM image of MoS_2 on the FTS/OTS square pattern where the color pattern is the graphical representation of the CPD. MoS_2 exhibits a larger CPD on the OTS compared to FTS with an absolute value difference of 0.2 eV. This result is confirmed by UPS measurements conducted on MoS_2 on FTS and OTS. The SECO and VB spectra can be found in Figure 2f. Values of $\Phi^{MoS_2}_{FTS} = 3.8$ eV, $\Phi^{MoS_2}_{OTS} = 4.0$ eV, $HIB^{MoS_2}_{FTS} = 2.0$ eV and $HIB^{MoS_2}_{OTS} = 2.0$ eV were extrapolated from the spectra. The difference of the work function of $\Delta\Phi^{MoS2}_{FTS-OTS} = -0.2$ eV is in excellent agreement with the KPFM results.

Figure 2j displays the PL-map of ML-MoS_2 on the OTS/FTS pattern, where the PL intensity is increased on FTS with respect to OTS. The averaged spectra (over a region of 20×20 μm^2) are displayed in Figure 2k where its PL intensity is $\approx$ ¾ lower on OTS compared to FTS. Because MoS_2 is a naturally n-doped semiconductor its PL intensity increases as the TMDC is p-doped. This is due to a decrease in negative trions and thereby an increase in radiative decay of excitons as seen in the deconvolution of the PL spectra (Figure S8, Supporting Information).[32–35,65,66] UPS measurements indicate a strong n-type character for MoS_2 on both OTS and FTS. The PL signal measured was therefore deconvoluted into the X^0 and the X^- peak for both spectra, where the X^- peak is redshifted with respect to the X^0 peak by 42 and 39 meV on OTS and FTS. Hence, the PL data confirms the p-doping effect of the FTS-SAM on ML-MoS_2, consistently with what is reported in literature.[18,19,24,54–57,67,68]

Table 2. Overview of Δ, the difference between ½ E_g and the HIB, the respective value for γ, and the resulting doping nature of the TMDCs on OTS and FTS.

	Δ [eV]	γ [%]	Doping nature
WSe_2 OTS	−0.05	−5	Intrinsic
WSe_2 FTS	0.23	20	p
MoS_2 OTS	−0.88	−78	n
MoS_2 FTS	−0.80	−67	n

As for WSe_2 the measurements were repeated on Al_2O_3 to ensure that the measured CPD originates solely from the interaction between MoS_2 and the SAMs and is independent from the substrate. Once again, the results on Al_2O_3 are in perfect agreement with those on Si/SiO_2 and are reported in the SI (Figure S7, Supporting Information).

The extended Schottky–Mott rule was applied to calculate the energy gap of MoS_2 as a function of the dielectric constant of the underlying SAMs, to predict the degree of doping induced by the latter. The energy level values for MoS_2 on the two different SAMs are reported in Table 1. We obtain two different values for $E_g(\epsilon_r)$ for MoS_2, 2.24 ± 0.04 eV for OTS and 2.40 ± 0.03 eV on FTS. With these values we calculate the parameter Δ, which is the difference between ½E_g and HIB, to be −0.88 eV for OTS and −0.80 eV for FTS. As a reminder, the closer the absolute value of Δ is to zero, the more intrinsic is the TMDC. A positive value corresponds to a p-doped TMDC, while a negative value to that of an n-doped TMDC. Thus, MoS_2 is less n-doped on FTS compared to OTS. These predictions are once again consistent with the observation in the PL-mapping (displayed in Figure 2j).

Figure 3a,b displays the energy level of WSe_2 and MoS_2, respectively, aligned at the E_F with FTS and OTS on Si/SiO_2. Applying the extended Schottky–Mott rule, E_g of WSe_2 on the OTS-SAM is smaller compared to that of WSe_2 on FTS by 0.2 eV. The HIB of 1.1 eV of WSe_2 on OTS places its E_F 0.05 eV above the middle of the band gap (½ E_g). For WSe_2 on FTS, E_F is positioned 0.23 eV beneath ½ E_g. For MoS_2, E_g on the OTS-SAM is smaller compared to that of MoS_2 on FTS by 0.15 eV. The HIB of 2.0 eV of MoS_2 on OTS places its E_F 0.88 eV above the middle of the band gap (½ E_g). For MoS_2 on FTS, E_F is positioned 0.80 eV above ½ E_g.

We introduce the variable γ (defined as $\frac{\Delta}{1/2E_g} \cdot 100$) to quantitatively describe the n-/p-character of WSe_2 and MoS_2 on the two different SAMs. For an intrinsic TMDC, γ equals 0%. For a n-doped TMDC, γ ranges from −100% to 0% (−100% corresponds to E_F pinned at the CB edge). For a p-doped semiconductor γ ranges from 0–100% (100% corresponds to E_F pinned at the VB edge). Applying this to WSe_2, its doping level is 20% on FTS and −5% on OTS. For MoS_2, it is −67% on FTS and −78% on OTS. An overview is given in **Table 2**. We conclude that the doping effect is stronger on WSe_2 compared to MoS_2. This is explained by the strongly locally bound electrons in MoS_2, arising from sulfur vacancies. The weaker, electrostatic forces of the SAMs have less effect on the modification of the electrostatic landscape with respect to WSe_2.

Figure 3c displays a cartoon of the correlation between the doping level and the PL intensity. FTS has a p-doping effect on both TMDCs, moving them further toward higher γ values (from left to right on the *x*–axis). This results in a lower PL intensity for WSe_2 on FTS compared to OTS, as its n-/p-nature changes from intrinsic to p-doped. For MoS_2, on the other hand, it results in a higher PL intensity on FTS compared to OTS, as it changes from n-doped to more intrinsic.

3. Conclusion

In conclusion, we presented a simple, low-cost procedure to achieve the local manipulation of the energy levels of TMDC MLs on the microscale level. This relies on the chemical functionalization of substrates such as SiO_2 with SAMs fabricated via micro contact printing. Through this technique and by selecting two different molecules for the SAMs (OTS and FTS), the surface substrate properties, such as its interfacial electric dipole and dielectric constant, can be controlled on microscale lateral dimension. By doing so, it is possible to engineer the surface properties of the substrate carrying the TMDCs and locally modify their electronic and optical properties. Furthermore, we have repeated our experiments also employing Al_2O_3 substrates and thereby demonstrating that the observed effects originate solely from the interactions between the TMDC and the SAMs, independent of the supporting substrate. Our results for WSe_2 and MoS_2 on patterns of FTS and OTS can be understood by considering not only the modification induced by the SAMs with respect to the surface dipole, but also the dielectric properties. We show that the different dielectric screening of the two SAMS results in a change in the electric band gap width of the two TMDCs. We thereby confirm the necessity of employing a more general expression of the Schottky–Mott rule for the correct prediction of the energy levels of TMDCs.

4. Experimental Section

Sample Cleaning: Highly doped Si wafer (Sigert Wafer, <100>, 525 µm thickness) with a thermal grown oxide layer (300 nm) were cleaned in an ultrasonic bath in deionized water, acetone, and isopropyl alcohol and then dried under nitrogen flow. Afterward, the substrates were plasma cleaned (0.35 mbar O_2, 5 min, Diener Plasma cleaner) to remove hydrocarbon contamination and activate the SiO_2 surface for SAM formation.

Microcontact Printing of SAMs: The stamp, employed for the µCP, were fabricated with a mixture of PDMS (Sylgard 184, Dow Corning) and a cross-linker (Sylgard 184, 10 m%). The two were mixed in a container and stirred for 1 min. The mixture was evacuated for 5 min at 10^{-2} mbar to remove air bubbles. Afterward, the mixture was cast over a stamp master, which was patterned with the features to be replicated on the stamp. The curing of the stamp occurred with a baking step (100 °C, 1 h). For the "SAM-ink," OTS (160 µL) was diluted in hexane (20 mL). The stamp was dipped into the ink (15 s), dried under nitrogen flow (30 s), and pressed onto the freshly plasma-cleaned substrates (10 s). The samples were placed on a hotplate (100 °C, 5 min), and cleaned with a Q-tip (dipped in hexene) followed by sonication in hexene and acetone. For the backfilling with FTS, the samples were placed in a FTS solution (60 µg FTS in 20 mL hexene) for 1 h, before being placed on the hotplate (100 °C, 10 min).

Chemical Bath Deposition of SAMs (For Reference Purposes): Cleaned Si/SiO_2 substrates (see above) were immersed overnight into an OTS solution in hexane (20 mM). The samples were placed on a hotplate (100 °C, 5 min), cleaned with a Q-tip (dipped in hexene) followed by sonication in hexene and acetone.

Metal Exfoliation Substrates: The fabrication of a smooth gold surface needed for metal-assisted exfoliation follows the procedure as previously

reported.[52,53] 150 nm Au and 1000 nm Cu were deposited on Silicon wafers (Sigert Wafer, <100>, 525 µm thickness) via physical vapor deposition (≈ 1.0 Å s^{-1} at 10^{-6} mbar). Glass substrates were fixed onto the metal-coated Si wafers with UV-curable epoxy resin (Osilla Encapsulation Epoxy S132).

Metal-Assisted Exfoliation: WSe_2 and MoS_2 (2D semiconductors, synthetic crystal) were cleaved with heat-resistant Kapton tape and transferred onto the freshly template-stripped metal substrate. After annealing (200 °C, 60 s) the Kapton tape was removed from the substrate, leaving ML-WSe_2 and ML-MoS_2 on the gold substrates.

Polystyrene-Assisted Transfer: WSe_2 and MoS_2 on Au were transferred following a reported process.[42] Polystyrene (Sigma Aldrich, $M_W \approx 280.000$, 90 mg mL^{-1} in toluol) was spin-coated (3000 rpm, 60 s) onto the TMDC/Au substrates following a curing step (80 °C, 10 min). The samples were left on a metal etchant (KI_2/I_2 Sigma Aldrich) until the polystyrene/TMDC film floated on top of the solution (≈ 48 h). To clean off etchant residue the film was transferred onto deionized water. For the transfer, the film was placed onto isopropyl alcohol and fished out with the target substrate. The samples were dried at room temperature (≈ 2 h) followed by an annealing step (150 °C, 30 min). The polystyrene was removed with hot toluene (90 °C) followed by rinsing with acetone and isopropyl alcohol.

Contact Angle Measurements: Static contact angle measurements were carried out (DSA100E from Krüss) using the sessile drop method with de-ionized water.

Scanning Force and Kelvin Probe Force Measurements: SFM/KPFM was performed in air with a Brunker Dimension Icon using PeakForce Tapping with a PFQNE-AL tip (Brunker).

Raman and Photoluminescence Measurements: Raman and PL spectroscopy were performed using a confocal microscope setup (Horiba Ltd.) with a 532 nm Laser excitation source and 20× objective (≈ 3 µm laser spot size) using an 1800 L mm^{-1} and 600 L mm^{-1} grating, respectively. The measurements were performed in ambient conditions.

Photoemission Measurements: UPS measurements were conducted using a monochromated helium discharge lamp (HIS 13 FOCUS GmbH, photo energy of 21.22 eV) in an ultrahigh vacuum system (1×10^{-9} mbar). A monochromator was used to eliminate visible light and reduce UV flux. All measurements were conducted in normal emission using a hemispherical electron analyzer (SPECS Phoibos 100). For the SECO spectra a bias (−10 V) was applied to the samples. XPS measurements were performed with a JEOL JPS-9030 (Jeol Ltd.) employing an Al electrode as photoexcitation source (hv = 1486.7 eV).

Scanning Electron Microscopy: SEM measurements were performed on a RAITH eLINE Plus microscope operating at 10 kV.

Statistical Analysis: SFM and KPFM images were processed with the Gwyddion software. For UPS and PL measurements the Igor Pro 7 software from wavemetrics was used.

Supporting Information

Supporting Information is available from the Wiley Online Library or from the author.

Acknowledgements

The authors would like to acknowledge Paul Zybarth and Bodo Kranz for their continuous support in the lab. The authors gratefully acknowledge financial support by the Deutsche Forschungsgemeinschaft through CRC 951 (Project number 182087777). This work was carried out in the framework of the Joint Lab GEN_FAB and was supported by the HySPRINT Innovation Lab at Helmholtz-Zentrum Berlin. The article processing charge was funded by the Open Access Publication Fund of Humboldt-Universität zu Berlin. The authors would like to thank Prof. Rabe for granting access to laboratory facilities. [Correction added on 22 August 2023, after first online publication: Projekt Deal funding statement has been added.]

Open access funding enabled and organized by Projekt DEAL.

Conflict of Interest

The authors declare no conflict of interest.

Data Availability Statement

The data that support the findings of this study are available from the corresponding author upon reasonable request.

Keywords

doping, MoS_2, self-assembled monolayers, transition metal dichalcogenides, WSe_2

Received: April 5, 2023
Revised: May 22, 2023
Published online: July 23, 2023

[1] D. Jariwala, V. K. Sangwan, L. J. Lauhon, T. J. Marks, M. C. Hersam, *ACS Nano* **2014**, *8*, 1102.
[2] G. Fiori, F. Bonaccorso, G. Iannaccone, T. Palacios, D. Neumaier, A. Seabaugh, S. K. Banerjee, L. Colombo, *Nat. Nanotechnol.* **2014**, *9*, 768.
[3] G. Wang, A. Chernikov, M. M. Glazov, T. F. Heinz, X. Marie, T. Amand, B. Urbaszek, *Rev. Mod. Phys.* **2018**, *90*, 021001.
[4] H. Guo, C. Lan, Z. Zhou, P. Sun, D. Wei, C. Li, *Nanoscale* **2017**, *9*, 6246.
[5] M. Y. Tsai, A. Tarasov, Z. R. Hesabi, H. Taghinejad, P. M. Campbell, C. A. Joiner, A. Adibi, E. M. Vogel, *ACS Appl. Mater. Interfaces* **2015**, *7*, 12850.
[6] H. Wang, L. Yu, Y. H. Lee, Y. Shi, A. Hsu, M. L. Chin, L. J. Li, M. Dubey, J. Kong, T. Palacios, *Nano Lett.* **2012**, *12*, 4674.
[7] X. Yang, K. Mohanram, Ambipolar Electronics, **2010**, https://doi.org/10.1002/scholarship.rice.edu/handle/1911/27467?show=full.
[8] Y. F. Lin, Y. Xu, S. T. Wang, S. L. Li, M. Yamamoto, A. Aparecido-Ferreira, W. Li, H. Sun, S. Nakaharai, W. B. Jian, K. Ueno, K. Tsukagoshi, *Adv. Mater.* **2014**, *26*, 3263.
[9] Y. Ren, X. Yang, L. Zhou, J. Y. Mao, S. T. Han, Y. Zhou, *Adv. Funct. Mater.* **2019**, *29*, 1902105.
[10] S. Hwang, H. Jinseong, L. Min-Hyun, B. Kyung-Eun, C. Yeonchoo, P. Seongjun, *Future Trends in Microelectronics* (Eds: S. Luryi, J. Xu, A. Zaslavsky), Wiley, New York **2016**, pp. 127-146.
[11] F. Bussolotti, H. Kawai, Z. E. Ooi, V. Chellappan, D. Thian, A. L. C. Pang, *Nano Futures* **2018**, *2*, 032001
[12] T. Mueller, E. Malic, *npj 2D Mater. Appl.* **2018**, *2*, 29.
[13] S. Katznelson, B. Cohn, S. Sufrin, T. Amit, S. Mukherjee, V. Kleiner, P. Mohapatra, A. Patsha, A. Ismach, S. Refaely-Abramson, E. Hasman, E. Koren, *Mater. Horiz.* **2022**, *9*, 1089.
[14] H. Tahara, Y. Kanemitsu, *ChemNanoMat* **2019**, *5*, 977.
[15] A. Raja, A. Chaves, J. Yu, G. Arefe, H. M. Hill, A. F. Rigosi, T. C. Berkelbach, P. Nagler, C. Schuller, T. Korn, C. Nuckolls, J. Hone, L. E. Brus, T. F. Heinz, D. R. Reichman, A. Chernikov, *Nat. Commun.* **2017**, *8*, 15251.
[16] Z. Qiu, M. Trushin, H. Fang, I. Verzhbitskiy, S. Gao, E. Laksono, M. Yang, P. Lyu, J. Li, J. Su, M. Telychko, K. Watanabe, T. Taniguchi, J. Wu, A. H. C. Neto, L. Yang, G. Eda, S. Adam, J. Lu, *Sci. Adv.* **2019**, *5*, eaaw2347.
[17] M. Sparks, G. K. Teal, Patent number:US2631356A, **1953**.
[18] Y. Li, C.-Y. Xu, P. Hu, L. Zhen, *ASC Nano* **2013**, *7*, 7795.
[19] H. Sojoudi, J. Baltazar, L. M. Tolbert, C. L. Henderson, S. Graham, *ACS Appl. Mater. Interfaces* **2012**, *4*, 4781.

[20] X. Sun, X. Wang, P. Wang, B. Sheng, M. Li, J. Su, J. Zhang, F. Liu, X. Rong, F. Xu, X. Yang, Z. Qin, W. Ge, B. Shen, *Opt. Mater. Express* **2017**, *7*, 904.
[21] E. Zojer, T. C. Taucher, O. T. Hofmann, *Adv. Mater. Interfaces* **2019**, *6*, 1900581.
[22] M. Salinas, *Interface Engineering with Self-Assembled Monolayers for Organic Electronics*, FAU University Press, Boca Raton, FL **2014**.
[23] B. Lee, Y. Chen, F. Duerr, D. Mastrogiovanni, E. Garfunkel, E. Y. Andrei, V. Podzorov, *Nano Lett.* **2010**, *10*, 2427.
[24] W. H. Lee, Y. D. Park, *Adv. Mater. Interfaces* **2017**, *5*, 1700316.
[25] B. de Boer, A. Hadipour, M. M. Mandoc, T. van Woudenbergh, P. W. M. Blom, *Adv. Mater.* **2005**, *17*, 621.
[26] J. Park, W. H. Lee, S. Huh, S. H. Sim, S. B. Kim, K. Cho, B. H. Hong, K. S. Kim, *J. Phys. Chem. Lett.* **2011**, *2*, 841.
[27] B. Liu, W. Zhao, Z. Ding, I. Verzhbitskiy, L. Li, J. Lu, J. Chen, G. Eda, K. P. Loh, *Adv. Mater.* **2016**, *28*, 6457.
[28] M. M. Ugeda, A. J. Bradley, S. F. Shi, F. H. da Jornada, Y. Zhang, D. Y. Qiu, W. Ruan, S. K. Mo, Z. Hussain, Z. X. Shen, F. Wang, S. G. Louie, M. F. Crommie, *Nat. Mater.* **2014**, *13*, 1091.
[29] J. Ryou, Y. S. Kim, S. Kc, K. Cho, *Sci. Rep.* **2016**, *6*, 29184.
[30] S. Park, T. Schultz, D. Shin, N. Mutz, A. Aljarb, H. S. Kang, C. H. Lee, L. J. Li, X. Xu, V. Tung, E. J. W. List-Kratochvil, S. Blumstengel, P. Amsalem, N. Koch, *ACS Nano* **2021**, *15*, 14794.
[31] M. Buscema, G. A. Steele, H. S. J. van der Zant, A. Castellanos-Gomez, *Nano Res.* **2015**, *7*, 561.
[32] D.-H. Kang, M.-S. Kim, J. Shim, J. Jeon, H.-Y. Park, W.-S. Jung, H.-Y. Yu, C.-H. Pang, S. Lee, J.-H. Park, *Adv. Funct. Mater.* **2015**, *25*, 4219.
[33] M. Amani, D.-H. Lien, D. Kiriya, J. Xiao, A. Azcatl, J. Noh, S. R. Madhvapathy, R. Addou, S. KC, M. Dubey, K. Cho, R. M. Wallace, S.-C. Lee, J.-H. He, J. W. Ager, X. Zhang, E. Yablonovitch, A. Javey, *Sci. Nanomater.* **2015**, *350*, 1065.
[34] Y. Li, Z. Qi, M. Liu, Y. Wang, X. Cheng, G. Zhang, L. Sheng, *Nanoscale* **2014**, *6*, 15248.
[35] S. Mouri, Y. Miyauchi, K. Matsuda, *Nano Lett.* **2013**, *13*, 5944.
[36] J. K. Hedlund, A. V. Walker, *Langmuir* **2020**, *36*, 682.
[37] D. M. Alloway, M. Hofmann, D. L. Smith, N. E. Gruhn, A. L. Graham, R. Colorado, J. V. H. Wysocki, T. R. Lee, P. A. Lee, N. R. Armstrong, *J. Phys. Chem. B* **2003**, *107*, 11690.
[38] H. Sugimuraa, K. Hayashia, N. Saitoa, N. Nakagirib, O. Takaia, *Appl. Surf. Sci.* **2002**, *188*, 403.
[39] M. A. Stoeckel, M. Gobbi, T. Leydecker, Y. Wang, M. Eredia, S. Bonacchi, R. Verucchi, M. Timpel, M. V. Nardi, E. Orgiu, P. Samori, *ACS Nano* **2019**, *13*, 11613.
[40] D. Jena, A. Konar, *Phys. Rev. Lett.* **2007**, *98*, 136805.
[41] Y. W. Yi, H. G. Robinson, S. Knappe, J. E. Maclennan, C. D. Jones, C. Zhu, N. A. Clark, a. J. Kitching, *J. Appl. Phys.* **2008**, *104*, 023534.
[42] A. Gurarslan, Y. Yu, L. Su, Y. Yu, F. Suarez, S. Yao, Y. Zhu, M. Ozturk, Y. Zhang, L. Cao, *ACS Nano* **2014**, *8*, 11522.
[43] Y. Song, R. P. Nair, M. Zou, Y. A. Wang, *Thin Solid Films* **2010**, *518*, 3801.
[44] M.-H. Jung, H.-S. Choi, *Korean J. Chem. Eng.* **2010**, *26*, 1778.
[45] Y. Wang, M. Lieberman, *Langmuir* **2003**, *19*, 1159.
[46] M. H. Park, Y. J. Jang, H. M. Sung-Suh, M. M. Sung, *Langmuir* **2004**, *20*, 2257.
[47] Y. X. Zhuang, O. Hansen, T. Knieling, C. Wang, P. Rombach, W. Lang, W. Benecke, M. Kehlenbeck, J. Koblitz, *J. Micromech. Microeng.* **2006**, *16*, 2259.
[48] Y. X. Zhuang, O. Hansen, T. Knieling, C. Wang, P. Rombach, W. Lang, W. Benecke, M. Kehlenbeck, J. Koblitz, *J. Microelectromech. Syst.* **2007**, *16*, 1451.
[49] J. Genzer, K. Efimenko, D. A. Fischer, *Langmuir* **2002**, *18*, 9307.
[50] Y. Gong, M. C. Wang, X. Zhang, H. W. Ng, B. D. Gates, *Langmuir* **2012**, *28*, 11790.
[51] R. E. Geer, D. A. Stenger, M. S. Chen, J. M. Calvert, R. Shashidhar, Y. H. Jeong, P. S. Pershan, *Langmuir* **1994**, *10*, 1171.
[52] M. Heyl, S. Grützmacher, S. Rühl, G. Ligorio, N. Koch, E. J. W. List-Kratochvil, *Adv. Mater. Interfaces* **2022**, *9*, 2200362.
[53] M. Heyl, D. Burmeister, T. Schultz, S. Pallasch, G. Ligorio, N. Koch, E. J. W. List-Kratochvil, *Phys. Status Solidi RRL* **2020**, *14*, 2000408.
[54] K. Yokota, K. Takai, T. Enoki, *Nano Lett.* **2011**, *11*, 3669.
[55] S. Kobayashi, T. Nishikawa, T. Takenobu, S. Mori, T. Shimoda, T. Mitani, H. Shimotani, N. Yoshimoto, S. Ogawa, Y. Iwasa, *Nat. Mater.* **2004**, *3*, 317.
[56] G. M. Ku, E. Lee, B. Kang, J. H. Lee, K. Cho, W. H. Lee, *RSC Adv.* **2017**, *7*, 27100.
[57] S. Najmaei, X. Zou, D. Er, J. Li, Z. Jin, W. Gao, Q. Zhang, S. Park, L. Ge, S. Lei, J. Kono, V. B. Shenoy, B. I. Yakobson, A. George, P. M. Ajayan, J. Lou, *Nano Lett.* **2014**, *14*, 1354.
[58] S. Park, T. Schultz, X. Xu, B. Wegner, A. Aljarb, A. Han, L.-J. Li, V. C. Tung, P. Amsalem, N. Koch, *Commun. Phys.* **2019**, *2*, 109.
[59] R. T. Tung, *Appl. Phys. Rev.* **2014**, *1*, 011304.
[60] S. Park, N. Mutz, T. Schultz, S. Blumstengel, A. Han, A. Aljarb, L.-J. Li, E. J. W. List-Kratochvil, P. Amsalem, N. Koch, *2D Mater.* **2018**, *5*, 025003.
[61] M. Takenaga, S. Jo, M. Graupe, T. R. Lee, *J. Colloid Interface Sci.* **2008**, *320*, 264.
[62] J. Colleta, M. Bonnierb, O. B. b, F. Rondelezband, D. Vuillaumea, *Microelectron. Eng.* **1997**, *36*, 119.
[63] H. B. Akkerman, R. C. G. Naber, B. Jongbloed, P. A. v. Hal, P. W. M. Blom, D. M. d. Leeuw, B. d. Boert, *Proc. Natl. Acad. Sci. USA* **2007**, *104*, 11161.
[64] R. D. Weinstein, J. Moriarty, E. Cushnie, R. Colorado, T. R. Lee, M. Patel, W. R. Alesi, G. K. Jennings, *J. Phys. Chem.* **2003**, *107*, 11626.
[65] D.-H. Lien, S. Z. Uddin, M. Yeh, M. Amani, H. Kim, J. W. Ager, E. Yablonovitch, A. Javey, *Science* **2019**, *364*, 468.
[66] Z. Luo, H. Jia, L. Lv, Q. Wang, X. Yan, *Nanoscale* **2020**, *12*, 17754.
[67] Z. Yan, Z. Sun, W. Lu, J. Yao, Y. Zhu, J. M. Tour, *ASC Nano* **2011**, *5*, 1535.
[68] J. Baltazar, H. Sojoudi, S. A. Paniagua, J. Kowalik, S. R. Marder, L. M. Tolbert, S. Graham, C. L. Henderson, *J. Phys. Chem. C* **2012**, *116*, 19095.